Journal of Fluids and Structures 56 (2015) 177–189

Contents lists available at ScienceDirect

Journal of Fluids and Structures

journal homepage: www.elsevier.com/locate/jfs

Effect of the curvature of elastic plates on the evolution of pulsatile flow fields

C. Hernández-Badillo [a], J.E.V. Guzmán [b,*], R. Zenit [c]

[a] Pemex Refinación, Av. Marina Nacional 329, Col. Verónica Anzures 11311, México D.F., Mexico
[b] Universidad Nacional Autónoma de México, Instituto de Ingeniería, Ciudad Universitaria 04510, Coyoacán D.F., Mexico
[c] Universidad Nacional Autónoma de México, Instituto de Investigaciones en Materiales, Ciudad Universitaria 04510, Coyoacán D.F., Mexico

ARTICLE INFO

Article history:
Received 30 September 2014
Accepted 9 May 2015
Available online 15 June 2015

Keywords:
Curvature
Flexible
Plate
Pulsatile
Flow

ABSTRACT

The flow field around curved elastic plates is experimentally investigated under pulsatile flow conditions. Particle Image Velocimetry (PIV) is used together with a *phase-locking* technique, in order to measure the velocities. Particular emphasis is placed on the viscous stresses and their local maxima, which are analyzed and discussed in detail. It is observed that the rate-of-strain, the vorticity, and the stress fields, attain higher local values as the curvature is increased. Moreover, the peak values of these quantities occur near the mid-cycle (i.e. at $t/T \sim 0.5$) and have slower decay rates in the case of curved plates. This study is motivated by the need to understand the fluid–structure interactions in the context of prosthetic heart valve design.

1. Introduction

The potential damage to the blood cells, caused by the interaction of the flexible leaflets with the pulsatile flow, is a major concern in the design of modern prosthetic heart valves (Yoganathan et al., 2004). In this regard Sallam and Hwang (1984) found that hemolysis may be induced at stress levels around 4×10^2 Pa. More recently Grigioni et al. (2001) suggested that the damaging stress values may actually be closer to 6×10^2 Pa, and that blood constituents could tolerate high levels longer than was previously thought. Accordingly, the viability of the prosthesis is determined by the evolution of the stress field which, in turn, is governed by the properties of the leaflets and the flow. Interestingly, despite the extensive research conducted over the past 50 years, the connection between such factors remains to be understood in detail (Yoganathan et al., 2004; Garitey et al., 1995; Butcher et al., 2011). This issue has been pointed out by Butcher et al. (2011), who suggested that geometrical aspects constitute the most important factor to be accounted for in the design criteria. Grigioni et al. (2001) have also underlined the importance of the curvature after considering its influence on the flow around two-leaflet valve prostheses. Although in their study these authors tested valves with rigid leaflets (the St. Jude type with flat leaflets, and the Sorin Bicarbon with cylindrical leaflets), their results indicated the existence of peak stress values produced downstream of the valve with curved leaflets. Such stresses were found to be significantly higher than those produced by the valve with flat leaflets. It is worth mentioning that profound dynamical differences distinguish the behavior of prosthetic valves from actual cardiac valves, since the later have to undergo a series of complex time dependent changes (e.g. in-plane and out-of-plane bending of the annulus,

* Corresponding author. Tel.: +52 55 5623 3600x8767.
E-mail addresses: chb@hotmail.com (C. Hernández-Badillo), eguzman@iim.unam.mx (J.E.V. Guzmán), zenit@servidor.unam.mx (R. Zenit).

http://dx.doi.org/10.1016/j.jfluidstructs.2015.05.006
0889-9746/

variations of radial and circumferential rigidities, and variations of the radii (Butcher et al., 2011)). Recently, López-Zazueta et al. (2011) showed experimentally that rigid leaflets induced higher stresses than flexible leaflets under the same nominal flow conditions. Thus, approaching the general bending characteristics of native valves seems to entail (almost exclusively) the introduction of biocompatible elastomers in current designs.

Besides the forgoing case other important problems in energy harvesting applications, aeroacoustics, aeroelasticity, and hydroelasticity, have inspired investigations involving similar systems. Of particular relevance are the plate-flow configurations previously studied by Peterson et al. (2009), Prince et al. (2010), and Kim et al. (2004). More concretely, Prince et al. (2010) have considered the use of active materials in the context of thrust production by inducing vibrations on slender strips. Their results highlight the relationship between tip displacement amplitudes, plate's aspect ratio and thrust production. With plates of high aspect ratio, the out-of-plane momentum fluxes caused by uneven deformations of the plates lead to a reduction of thrust. A comprehensive account on energy harvesting applications is given by Porfiri and Peterson (2013). The interactions between Ionic Polymer Metal Composites (or IPMC) and oscillating flows are widely discussed, and the effects caused by vortex induced damping of the plates under severe oscillations are underlined. Optimal energy extraction is observed to occur when flow oscillations match the resonant frequencies of the plates. For an insightful discussion about the three-dimensional effects in the vicinity of a vibrating slender plate in a quiescent fluid, the reader is referred to Kim et al. (2004). Vortex shedding from the tip of the plate causes a rich flow evolution downstream from the plate. Furthermore, during the formation of such vortices, the effect of the no-slip condition at the sidewalls leads to a transversal flow that feeds fluid into the evolving vortex. The vortex detaches and proceeds to develop downstream in a process that resembles the one described in the present study. The important effect of nonlinear damping of slender flexible plates oscillating in quiescent fluids is further investigated by Bidkar et al. (2009). In this context, damping is found to increase with the amplitude of the vibrations and, moreover, it is associated with an out-of-phase interaction between the structural accelerations and the local fluid accelerations.

The fluttering phenomenon caused by axial flows has also become an attractive subject due to its numerous applications involving micro-mechanical devices, wing design, marine structure design, and biomechanics (e.g. Phan et al., 2011; Facci and Porfiri, 2013). Other studies in this field have focused on the fluttering of plates in high speed flows, or on the deflection of plates due to normal flow and wave impacts (e.g. Yamaguchi and Yokota, 2000; Faltinsen, 2000; He and Kashiwagi, 2010). Non-linear excitations, resonances and oscillations of flexible plates interacting with fluids have also been investigated, both from the experimental and numerical points of view (e.g. Ihara and Watanabe, 1994; Carra et al., 2013; Arellano Castro et al., 2014). Fundamental problems, such as the stability and vibration modes of plates and beams acted upon by axial flows, have been considered previously by Taylor and Ohkusu (2000), Gluck et al. (2001), Eloy et al. (2008), Howell et al. (2011), and Tubaldi and Amabili (2013). In addition, the non-linear behavior and coupled interactions of parallel plates confining axial flows have prompted complementary work due to their practical applications (e.g. Lucey et al., 1997; Jang et al., 2013).

Bearing a closer relation with the present study are the numerical investigations by Lee and Lee (2012), and by Gluck et al. (2001), on the deflection and oscillation modes of flexible plates interacting with normal flows. The investigation by Gosselin et al. (2010) on the reduction of drag by reconfiguration of flexible plates presents relevant insights about their bending characteristics under steady flows. More concretely, the flexural rigidity was observed to increase the drag for a flow acting perpendicularly on the plate's surface. Notwithstanding, our study differs from Gosselin's work in three major ways: (a) a transversal curvature spans the width of the plate (i.e. there is only one plane of symmetry), (b) the interaction with pulsatile flows is considered, (c) the focus is placed on the evolution of the flow around the plate. In addition, the results of the numerical investigation by Pedrizzetti and Domenichini (2006) concerning the problem of flow-driven opening of rigid leaflet valves are relevant to our study. Some features of the flow field around hinged plates which are impulsively started resemble the ones reported here. In particular, the jets inducing the formation of swirling wakes downstream from the plate are remarkably similar in both cases. It should also be remarked that the present study is a continuation of the work by Ledesma-Alonso et al. (2014), who investigated the effect of the material properties of a model valve with flat leaflets. The authors found that other geometrical factors, such as the plate's length and thickness, have a strong influence on the performance of the valve. Nevertheless, it was also clear that a separate study was needed in order to isolate the effects associated with the curvature. As a result, we set out to experimentally investigate the distinctive features of the flow that can be attributed exclusively to the curvature. It must be emphasized, however, that in contrast to the study by Ledesma-Alonso et al. (2014) the present configuration does not represent a model valve because it consists of a single plate. In the present study the strains, the vorticity and the viscous stresses, are directly determined from the velocities measured around plates with different curvatures. The mean evolution of these fields is compared and discussed, thereafter.

2. Experimental procedures

2.1. The setup

A schematic view of the test section of the apparatus is shown in Fig. 1. The flow system was carefully configured in the fashion of the so-called Windkessel (or wind cage) model, which is normally used in laboratory representations of the human circulatory system (e.g. Diourté et al., 1999). Its squared, cross-section channel was made of transparent acrylic to allow proper visualization. Two clamps with the prescribed curvature could be fitted inside the channel to hold in place the plates. Coupled to the inlet of the test section, a special chamber containing small spheres ensured a uniform flow upstream from the plate.

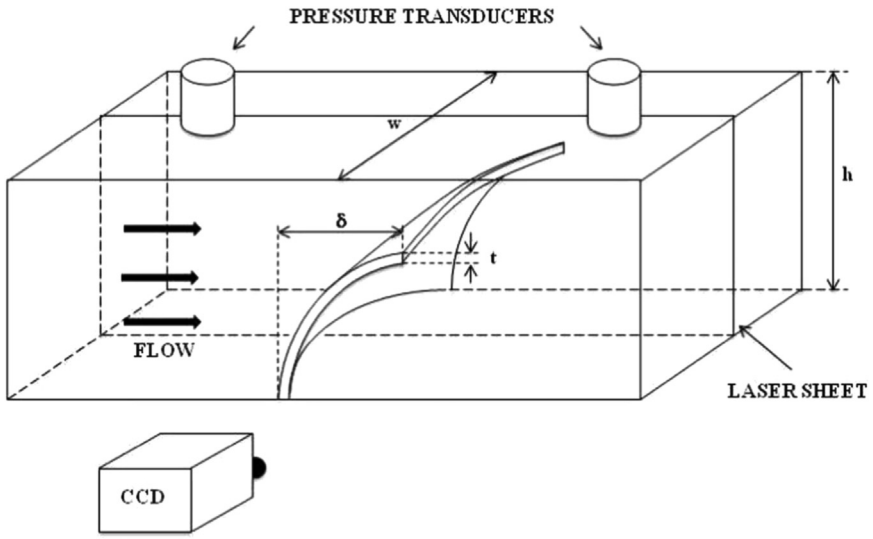

Fig. 1. Test section of the experimental apparatus. The flexible plates were located nearly halfway between the inlet and the outlet, and were attached by means of specially designed holding clamps that remained flushed with respect to the channel's inner wall.

Downstream, the channel was connected to a compliance tank that emulated the behavior of elastic vessels. It should be noted that without this last item, the coupled dynamical response of the fluid and the plate would significantly differ from those flows normally produced in prosthetic valves.

Predefined pulsatile flow rates were supplied by a Harvard 1423-55-3305 series pump, according to

$$G = V_s f. \tag{1}$$

An independent control of the stroke (or displaced) volume V_s, and the pumping frequency f, allowed for a variety of flow conditions to be explored. Table 1 summarizes the ranges of variation of these parameters. A one-directional circulation of the fluid was enforced with a check-valve, while fine adjustments to the flow were handled with a needle valve. Although the pump produced regular flow pulses, the compliance tank had a tendency to introduce a spring-damper effect that created a time delayed counter-pressure in the flow. These two effects combined to form the flow driving the plates, which was locally studied by means of the PIV measurements. Pressures were measured, simultaneously, via two transducers installed on either side of the leaflet: an Omegadyne PX-309030A5V located upstream, and a Kobold KPK-30/302227 located downstream.

The flexible plates (of length $L = 2.6 \times 10^{-2}$ m, width $W = 4.8 \times 10^{-2}$ m, and thickness $h = 4 \times 10^{-4}$ m) were given specific curvatures by means of appropriately shaped cuts performed on the holding clamps. The material and geometrical properties of these plates are summarized in Table 2. A gap of approximately 1.5 mm was left between the lateral edges of the plates and the walls to prevent frictional effects. Four curvatures were tested, and each curved plate was subjected to 12 different pulsatile flow conditions. All parameter combinations then yielded 48 experimental series, with 200 cycles analyzed per series.

For convenience water was selected as the working fluid, and the comparison focuses exclusively on silicon plates with two curvatures: $\kappa = 0.0\ \mathrm{m}^{-1}$ and $\kappa = 2.0\ \mathrm{m}^{-1}$. Plots containing collective results for all curvatures are presented in the discussion section to illustrate general trends.

It should be emphasized that the focus of the study was placed on the influence of the curvature on the flow field around the plate. A simplified model would presumably allow for a clearer identification of those flow features that could be attributed to the curved plates alone. Therefore, a single plate model was preferred in order to eliminate other coupled interactions related with a two-leaflet valve configuration.

2.2. Measurement techniques

The velocity field in the vicinity of the leaflet was measured by means of a Particle Image Velocimetry System (see Fig. 1). In the implemented scheme all measurements were carried out with a phase-locking technique, by which synchronized snapshots could be taken at particular instants of each cycle. Based on sensitivity tests it was determined that 200 samples per series were sufficient for adequate statistical convergence (a compromise was sought between the amount of information to be handled, and the quality of the results). Therefore, since the cycle's period T was subdivided into 10 equal parts, a total of 2000 snapshots of the vector field were analyzed statistically.

An Eulerian description of the flow was obtained by seeding the fluid with silver coated, hollow, glass spheres with a mean diameter of 10 μm, and a relative density $\gamma \simeq 1$ (i.e. tracers were neutrally buoyant). These tracer particles were then illuminated with a light sheet, which was emitted at a wavelength of 532 nm from a Nd-YAG laser (LDY301-PIV). A CCD Speed Sense Phantom camera was synchronized with the laser for optimal particle displacement measurement. In this

Table 1
Pump parameter values considered in the experiments.

Parameter	Values	Unit
Pumping frequency (f)	40, 60, 70, 90 0.67, 1.0, 1.17, 1.5	pulses/min (ppm) Hz
Stroke volume (V_s)	30, 45, 60 3.0, 4.5, 6.0	cm^3/pulse $\times 10^{-5}$ m^3

Table 2
Material and geometrical properties of the silicon plates.

Plate no.	κ (m^{-1})	ρ ($\times 10^3$ kg/m)	E ($\times 10^6$ Pa)	I ($\times 10^{-12}$ m^4)	D (kgm^3/s^2)	h ($\times 10^{-4}$ m)	L ($\times 10^{-2}$ m)
S0	0.0	1.07	2.15	0.025	$5.39\times10-7$	4.0	2.6
S1	1.0			1.03	$2.22\times10-5$		
S2	2.0			2.27	$4.90\times10-5$		
S3	4.0			2.03	$4.35\times10-5$		

scheme, two consecutive snapshots were taken with a 5 μs time lapse between them, and the resulting 532 × 532 pixel image was divided into 64 × 64 pixel interrogation windows (IW) with a 30% overlap. In order to decrease the signal-to-noise ratio, as well as the displacement-to-IW ratio, the concentration of particles was increased to produce a minimum of 10 particles per IW. Their displacements were then determined by cross-correlating their positions in two consecutive snapshots. These procedures allowed for a global space wise resolution of 1.3×10^{-3} m/pixel. It is worth mentioning that previous studies have demonstrated the adequacy of this resolution level for determining the average primary field, as well as the derived fields (Ledesma-Alonso et al., 2014). Within this framework the maximum uncertainties are below 12.3%.

Hence, local average values for the k-th velocity component were estimated according to

$$\overline{v_k(\mathbf{x},\tau_j)} = \frac{1}{N}\sum_i v_k\left[\mathbf{x}, \tau_j' + (i-1)T\right], \tag{2}$$

with the sum taken over the total number of cycles per experiment: $i = 1, 2, \ldots, N$. The quantity $\tau_j' + (i-1)T$ is the *phase-locked* time. It specifies the precise moment inside the interval $0 \le \tau_j' < T$, of each subsequent cycle of period T, at which values of v_k are measured. The **x** appearing in this expression represents the Eulerian position.

Fig. 2 illustrates the nature of the velocity fields around the plate. The arrows indicate the magnitude and direction of the velocities at different points. For instance, in Fig. 2(a) we observe a quiescent fluid around the plate, while Fig. 2(b) shows a strong jet produced under steady state flow conditions. These fields are time independent, so no additional features are developed subsequently. In contrast, Fig. 2(c) and 2(d) illustrates the characteristic flowfields observed at two different times in the pulsatile regime. A vortex-like structure is clearly seen in the first snapshot, while a jet appears as the most prominent feature in the second snapshot. It should be remarked that both states result from a continuous evolution of the flowfield during the cycle.

3. Description of the flow structure

3.1. Structure of the velocity field

Only the average field values are considered in the following sections. This may be justified on the grounds that the fluctuating part of the velocity field vanishes when averaging over a sufficiently large number of cycles (i.e. $\overline{\mathbf{v}^*(\mathbf{x},\tau_j)} \to 0$ as $N \to \infty$); thus,

$$\mathbf{v}(\mathbf{x},t) \approx \overline{\mathbf{v}(\mathbf{x},t)} = \sum_k \hat{e}_k \overline{v_k(\mathbf{x},\tau_j)}, \quad j = 1, 2, \ldots, m. \tag{3}$$

Here the unit vectors $\hat{e}_k$ define the basis of the Cartesian system in two dimensions ($k = 1, 2$) located on the channel's mid-plane, and m is the number of time partitions. As it was stated above, in this study we consider $m = 10$ partitions of the cycle's period T.

The images presented in Fig. 3(a) correspond to a flat plate and illustrate the characteristics of the reference flow. Snapshots corresponding to times $t/T = 0$ and $t/T = 1$ are not included because the corresponding flow states are almost identical. Relevant flow features start to become discernible at $t/T = 0.1$. The coupled action of the pump and the compliance tank introduces an offset between the pressure and the velocity fields. This is a relevant feature of pulsatile flows through elastic vessels, such as the circulatory system (e.g. Thiriet, 2008). At the beginning of the cycle the pump

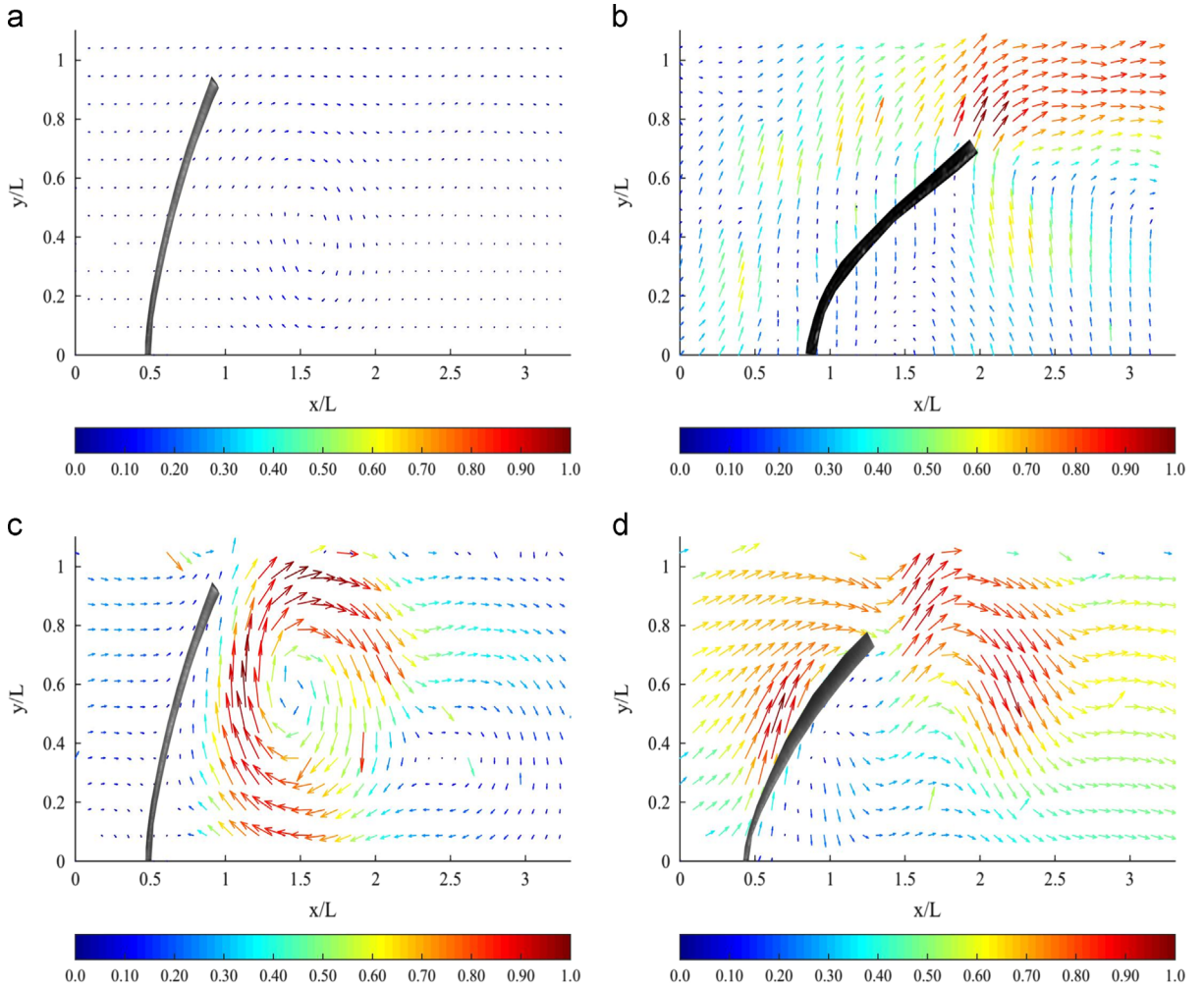

Fig. 2. Characteristics of the velocity fields. Figure (a) shows a quiescent fluid, while (b) shows the time independent flowfield in a steady state regime. Figures (c) and (d) correspond to the pulsatile flow regime, and illustrate two states of a flowfield that evolves permanently during the cycle.

progressively increases the upstream pressure, until it overcomes the pressure built up inside the compliance tank during the previous cycle. Beyond a certain pressure threshold the fluid starts moving rapidly through the channel. This effect can be inferred directly from the pressure plots (Fig. 4) and the velocity plots (Figs. 7 and 8), where it may be seen that both quantities grow and decrease at different times t/T.

Accordingly, the fluid–structure interaction has two important moments. There are stages where the pressure dominates (i.e. when the flow is impulsively started, and when the flow slows down). Swirling motions are formed during this stages, and are easily observed to evolve at times $t/T=0.1$ and $t/T=0.7$. At this point it is important to remark that the formation of swirls is necessary to an adequate operation of the valve (Butcher et al., 2011; Yoganathan et al., 2004). However, persistent circulations may also extend the residence times in regions with high shearing.

Jets, on the other hand, are characteristic of intermediate stages where the process is dominated by the fast motion of the fluid. Starting from $t/T=0.3$ the main flow is stronger in the axial direction, such that the conditions promoting the appearance of secondary eddies vanish. Jets are thus formed that prevail until the flow slows down during the diastolic phase. By $t/T=0.5$, the flow has slowed down enough to favor the formation of additional secondary eddies. Progressively, these eddies grow in strength and merge to form the full swirling motion that can be clearly seen at $t/T=0.9$. The plate has completely returned to its undeformed state by $t/T=1$. It is noted that high velocities are produced near the wall and the plate by neighboring swirls. Since any particle therein contained would be overly stressed and its residence time would be vastly increased, regions of this sort pose a greater damaging potential for soft particles. Such considerations are quite relevant in the context of artificial valve design to avoid blood damaging processes.

In terms of the strains produced in the fluid, it is noteworthy that the highest values would occur within a layer formed by the jet impinging on the upper wall of the channel (Fig. 3(a)). Clearly this layer is not continuous in the axial direction, so that fluid particles moving in its interior would be subjected to alternating high and low deformations for a time spanning

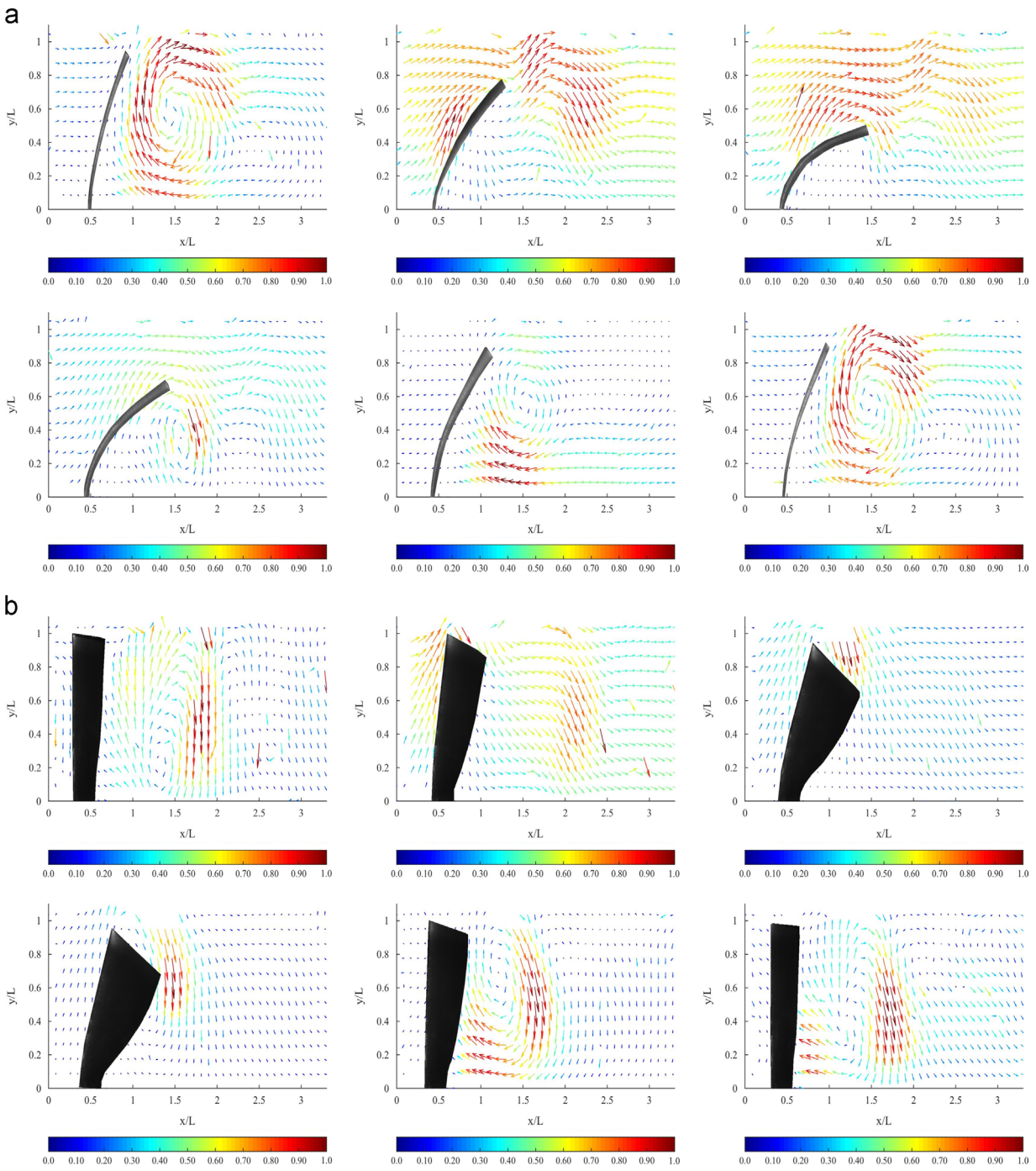

Fig. 3. Velocity fields generated around flat plates (a) and curved plates (b), with $\kappa = 0.0\ \mathrm{m}^{-1}$ (S0) and $\kappa = 2.0\ \mathrm{m}^{-1}$ (S2), respectively. The flow output corresponds to $f = 70$ ppm and $V_s = 45\ \mathrm{cm}^3$.

approximately 15% of the cycle's period. Two other layers are additionally formed: one develops along the upstream surface of the plate, from $t/T = 0.0$ to $t/T = 0.3$, and another one appears on the lower wall just downstream from the plate at $x/L \approx 2$. Both wall layers develop up to times $t/T \approx 0.4$–0.5, when the maximum deflections occur. Meanwhile, the plate's surface layer evolves into a spot-like region that concentrates fluid of relatively moderate strain amplitude. Although the spot does not detach from the plate, its shape is nonetheless modified by the presence of stronger eddies interacting with it. This effect presents itself as a distorted filament at $t/T = 0.5$. As soon as the diastolic phase commences ($t/T = 0.5$) a lower patch exhibiting high strains is induced at $x/L \approx 1.3$. Just a moment later, from $t/T = 0.7$ onwards, the leaflet moves back to its undeformed state, while the upper wall layer slowly decays for the remaining part of the cycle.

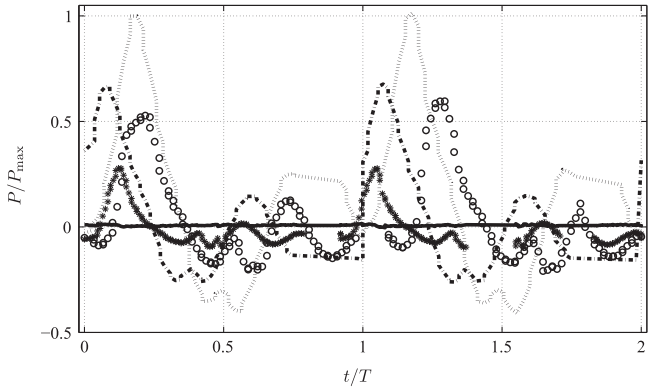

Fig. 4. Pressure difference across the valve for two cycles. Curves correspond to the output frequencies $f=$ 40 ppm (⋆⋆⋆), 60 ppm (○○○), 70 ppm (·− · −·), 90 ppm (·····). The difference between the upstream and downstream pressures is represented by the solid curve (−).

Now if the curvature is increased to $\kappa = 2.0\ \mathrm{m}^{-1}$ (plate S2), all other conditions kept constant, we have the evolution illustrated by Fig. 3(b). Clearly, the previously described flow features are less evident in this case. Nevertheless, plates with increased rigidities produce quite discernible flow structures. For instance, a filamentary distribution of strained fluid appears connected to the upper layer. Strains within this region increase until $t/T = 0.4$; meanwhile the locations of the upper wall layer and the filament remain approximately stationary throughout this part of the cycle. On the other hand, the lower layer evolves in a way similar to the reference flow. For intermediate times two spots with significant strains can be identified: one just above the outer edge of the plate and one located at $x/L \approx 1.2$, close to the plate's attachment point. These strain regions are dissipated quite rapidly. Apart from the very small deflections sustained by curved plates (in contrast with the flat plate case), their induced strains have larger absolute values.

A few comments are necessary concerning the flow around the plate's edges and the finite size of the channel. First, the size of the gap ξ between the lateral walls and the plate's edge is small when compared with the characteristic lengths of the plate: $\xi/L \sim \xi/W \sim 10^{-1}$. When the flow accelerates the characteristic cross-sectional size of the swirls, ζ say, is also typically small (i.e. $\zeta \sim h$). Meanwhile, the boundary layers grow according to $\delta_b \sim \sqrt{\nu\, t}$ (for $0 \le t < 0.1T$ this implies $\delta_b \sim 10^{-4}$ m). Evidently, the swirls and the wall boundary layers will interact to some extent, but we notice that $\zeta/\xi \sim 10^{-1}$ and also that $\delta_b/\xi \sim 10^{-1}$, according to the previous statements. Hence, edge related effects would tend to evolve with relative independence from the boundary layer during the initial stage of the flow.

Secondly, in addition to the slow viscous growth-rates of the boundary layers and the eddies, the rapid bending of the plate contributes largely to the decrease of the net circulation within the edge swirls. Since $\delta_b/W \sim \zeta/W \sim 10^{-2}$, the evolving swirls do not span the sufficient plate's area, nor have the strength, to produce perceptible three-dimensional structures in the region of interest. Owing to the same effects the upper part of the swirl eventually detaches from the plate's edge and evolves into the full vortex-like structure previously discussed. Finally, it should also be noted that local, out-of-plane twisting of the plates was not observed during the experiments (except for a slight inwards deflection at the tips of the plate with highest curvature towards the mid-cycle).

3.2. Structure of the vorticity field

The rate-of-strain tensor **S** and the rotation tensor **R** are key to understanding the local structure of the flow field. In particular, viscous stresses are proportional to **S**, while the swirling motions are related to **R**. These two quantities correspond, respectively, to the symmetric and anti-symmetric parts of the velocity gradient tensor:

$$\mathbf{S} = \frac{1}{2}\left[\nabla\mathbf{v} + (\nabla\mathbf{v})^T\right] \tag{4}$$

and

$$\mathbf{R} = \frac{1}{2}\left[\nabla\mathbf{v} - (\nabla\mathbf{v})^T\right]. \tag{5}$$

Their magnitudes can be estimated by means of the norms

$$\|\mathbf{S}\| = \left(\mathbf{S}{:}\,\mathbf{S}^T\right)^{1/2}, \quad \text{and} \quad \|\mathbf{R}\| = \left(\mathbf{R}{:}\,\mathbf{R}^T\right)^{1/2}. \tag{6}$$

Furthermore, the vorticity also follows directly from Eq. (5) since, by definition,

$$\omega_z = \left(\frac{\partial u_y}{\partial x} - \frac{\partial u_x}{\partial y}\right). \tag{7}$$

The vorticity enables a clearer identification of large and small eddies in the flow, and indicates the strength of the local rotations.

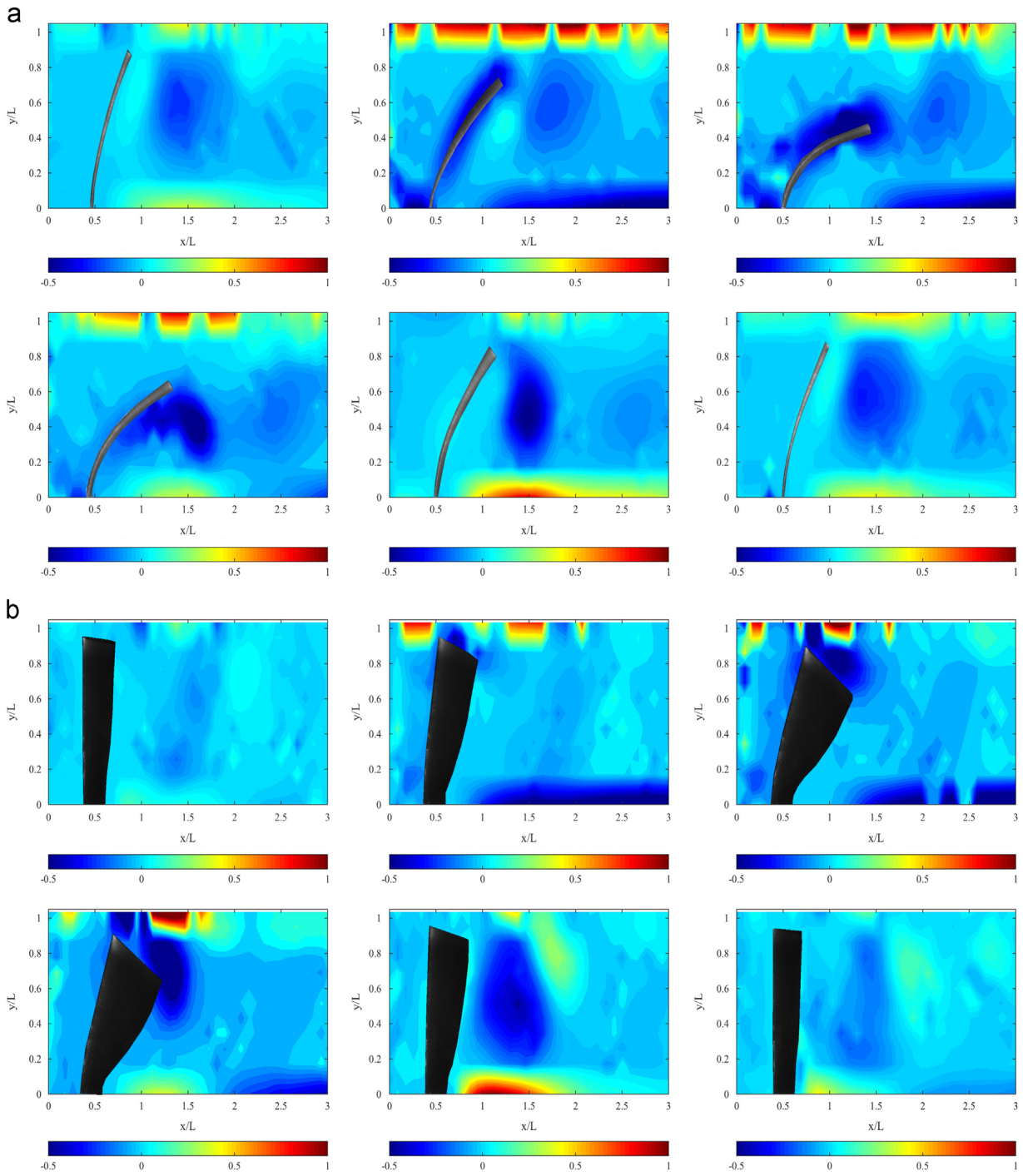

Fig. 5. Vorticity field ω_z. The sequence of images in (a) and (b) show the evolution related with plates whose curvatures are $\kappa = 0.0\ \mathrm{m}^{-1}$ (S0) and $\kappa = 2.0\ \mathrm{m}^{-1}$ (S2), respectively. The flow output corresponds to f=70 ppm, and V_s=45 cm^3.

Fig. 5(a) and 5(b) illustrates, respectively, the evolution of ω_z for plates S0 and S2. In the first case a rather compact clockwise circulation is generated downstream (immediately behind the plate) when the cycle begins. This circulation is advected with the main flow, while at the same time the layer developing on the upstream surface of the plate generates a new swirl that is, eventually, shed to the wake (from $t/T = 0.3$ to $t/T = 0.5$). On the other hand, the shear layer at the upper wall is characterized by a strong counter-clockwise vorticity. The combined action of these two patches is represented by the axial jet emerging from the reduced cross section between the upper plate's edge and the wall. Hence, any particle located near the line separating these two circulations would be rapidly convected downstream. At $t/T = 0.5$ a new circulation is formed from behind the plate (i.e. on the

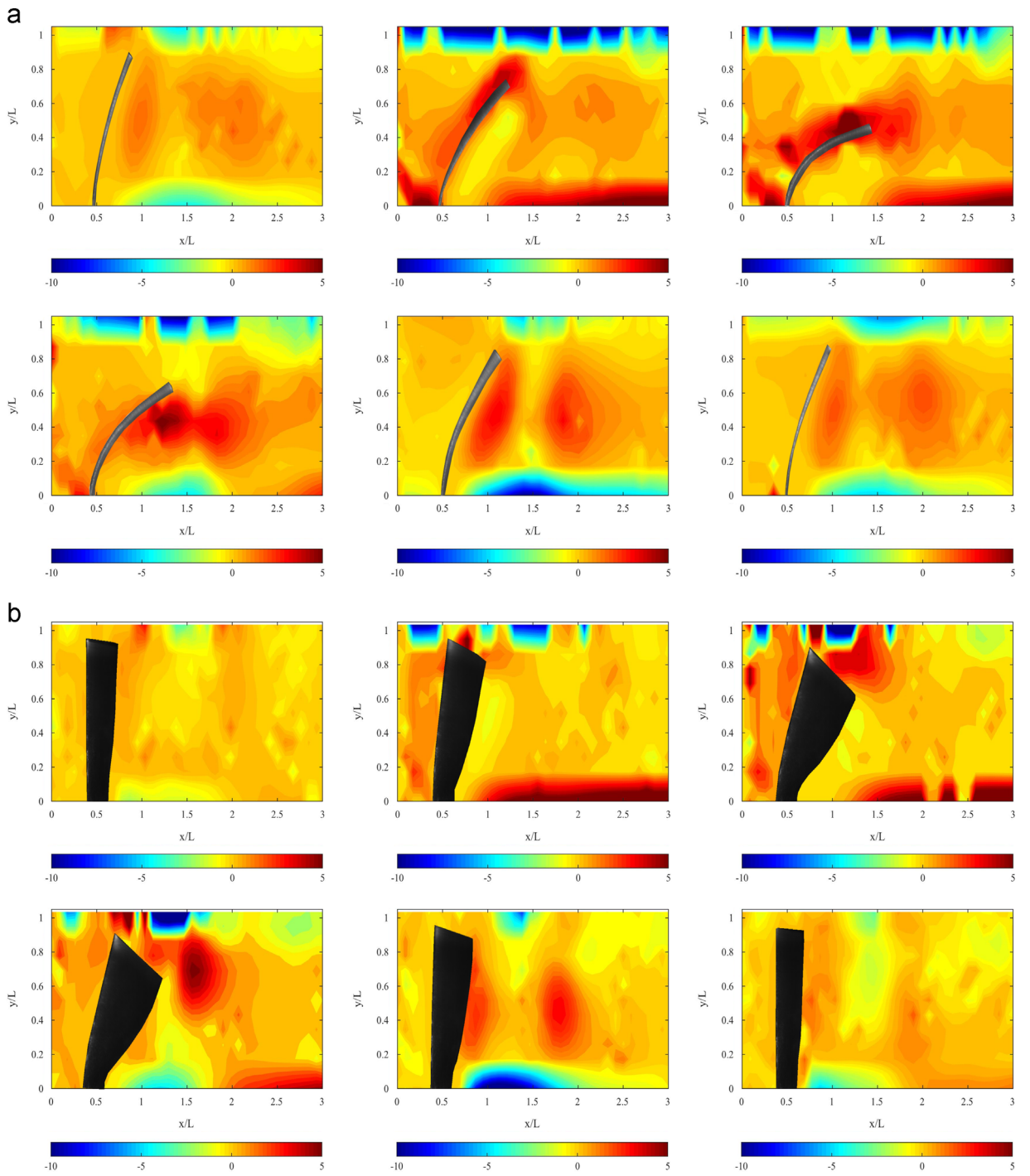

Fig. 6. Stress field Σ. The sequence of images in (a) and (b) correspond to plates with curvatures $\kappa = 0.0\ \mathrm{m}^{-1}$ (S0) and $\kappa = 2.0\ \mathrm{m}^{-1}$ (S2), respectively. The pulsatile output corresponds to f=70 ppm, and V_s=45 cm^3.

downstream side); this secondary flow separates from the plate and remains more or less stationary at $x/L \approx 1.5$ due to the diastolic flow. It is important to remark that this circulation favors the appearance of two vorticity layers at the upper and lower walls. Their strengths are a clear indication of the large amount of angular momentum contained within the main circulation. Evidently, the strength of the lower layer is much larger than in its counterpart ($t/T = 0.7$), because it is farther apart from the flow through the aperture. During the final stage of the cycle these two layers are still present, but in a much weaker form.

With a higher curvature the entire flow field becomes more irregular, showing smaller scale eddies everywhere (Fig. 5(b)). Still, some large circulations are observed; most prominently, the patch of vorticity generated at the tip of the

leaflet that develops into a full vortex from $t/T=0.3$ to $t/T=0.7$. A layer of high amplitude counter-clockwise vorticity is formed, again, by the large vortex shed from the tip of the plate ($t/T=0.4$). This induced layer is quite irregular. Apparently, the velocity of the main flow is insufficient to detach and transport this vortex-like structure along with the main stream (as can be seen in the image subsequence for $t/T=0.4, 0.5, 0.7$). As a result a considerable mass of rotating fluid is retained behind the plate, located approximately at $x/L=1.3$. In analogy with the reference case, a secondary layer is induced on the lower wall by this circulation. Towards the end of the cycle this swirl slows down and dissipates.

3.3. The viscous stress field

For Newtonian fluids with dynamic viscosity μ, the shearing components of the stress tensor are linearly related with the components of the rate-of-strain tensor by

$$\boldsymbol{\Sigma}=2\mu\mathbf{S}. \tag{8}$$

As before,

$$\|\boldsymbol{\Sigma}\|=\left(\boldsymbol{\Sigma}:\boldsymbol{\Sigma}^{T}\right)^{1/2} \tag{9}$$

allows for an estimate of their respective magnitudes at every point in the fluid. We focus exclusively on viscous stresses, since the compressive effects have been found to be less relevant in those cases motivating the present study (López-Zazueta et al., 2011). Moreover, in this way the effects of the flow are emphasized (i.e. shearing effects are only possible when the fluid is in motion).

Keeping these stresses below certain threshold levels in the periphery of the flexible plates is of paramount importance in the design of prosthetic heart valves (Giersiepen et al., 1990; Hellums, 1994; Bluestein et al., 2000). In addition, (intermittent) exposure to high stress levels should occur for the least amount of time, in order to avoid cumulative trauma effects (López-Zazueta et al., 2011). Fig. 6(a) and (b) shows the complex arrangement of the stress distribution for plates S0 and S2. Since $\boldsymbol{\Sigma}\propto\mathbf{S}$, the evolution of the stress field coincides with the description already presented in relation with the strains. Therefore, we discuss only the stress levels attained in different parts of the fluid. In particular for the flat plate ($\kappa=0.0\ \mathrm{m}^{-1}$) two intense stress regions are identified, at $x/L=1.0$ and $x/L=2.5$, during the initial stages of the cycle. Stress levels at these locations are observed to be in the intermediate range, namely: $0.02\leq\Sigma\leq0.025$ Pa. Furthermore, the stresses inside the upper wall layer attain the highest absolute values observed during the cycle, with $\Sigma\approx0.06$ Pa during the time interval $0.3\leq t/T\leq0.5$. Although the upper layer continues to be affected by local eddies it retains considerable damaging potential within the smaller patches. Meanwhile, the stresses associated with the layers developing on both faces of the plate have values within the interval $0.02\leq\Sigma\leq0.025$ Pa. By $t/T=0.5$ the layers detach from the plate and travel into the mainstream, giving way to the formation of the circulations observed therein (with $\Sigma\leq0.01$). Interestingly, the maximum stresses are not confined in the cores of the vortices, but are rather located on their periphery (possibly due to relative motions with respect to other regions of the flow field).

In contrast, a more complex stress distribution results when a curved plate ($\kappa=2.0\ \mathrm{m}^{-1}$) is considered. First we note that the stresses induced during the first half of the cycle are higher than those observed during the second half of the cycle (a similar concern would be raised in the case of the flat plate). Second, the large vortex-like patterns previously described are almost nowhere present, except for a short time around the mid-cycle (at $t/T=0.5$) and at the tip of the plate. For the reasons already mentioned, the layers induced by the ejected fluid at the upper edge still concentrate the highest stress levels (with absolute values $\Sigma\geq0.06$ Pa). The bottom wall layer and the small eddy that detaches from the plate evolve with moderate stress values in the range $\Sigma\sim0.02$. This occurs from $t/T=0.4$ to $t/T=0.7$, while the wall layer is noticed to span a larger axial distance from $1\leq x/L$ (almost at the base of the plate). Intermittent spikes of high and low stress values show up in the wake, as well.

4. Discussion

4.1. Effect of the curvature in the pulsatile regime

We begin by characterizing the time-scale of the pulsating flow as $t_f\sim1/f$. The relaxation time for a plate moving in the fluid may be obtained from the corresponding equation of motion; accordingly we have $t_p\sim\sqrt{\rho_p\ V_p\ L^3/(EI)}$ (where ρ_p is the material's density, V_p the plate's volume and L its length). In turn, the above scales imply $t_p/t_f\sim10^{-3}$–10^{-2} for low frequency pulsating flows. During the experiments the plates were observed to have more than sufficient time to internally adjust to the varying flow conditions (i.e. deflections occurred quite evenly throughout the cycle). Moreover, at intermediate times when the plate approaches its ultimate deflection state the flow dynamic force, $F_f\sim\rho U^2\ L^2$, becomes comparable to the plate's restoring force $F_p\sim EI/L^2$ (considering that the velocity scales as $U=f\ L$). As a result, a streamlined reconfiguration of the sort studied by Gosselin et al. (2010) would take place during the mid-part of the cycle for low curvature plates.

In addition, the distinctive spikes observed in the velocity magnitude (within the $0.3\leq t/T\leq0.5$ interval) are analogous to the ones observed by Grigioni et al. (2001) for rigid leaflets. Fig. 7(a) shows maximum velocity values for the flat plate S0, while Fig. 7(b) belongs to the curved plate S2. The frequencies under consideration are $f=40, 60, 70, 90$ ppm. It is clear from the comparison between these two cases that higher curvatures induce higher speeds. Interestingly, the velocities seem to approach the same peak value as $f\rightarrow90$ ppm, regardless of the plate's curvature. The velocity dependence on f is also

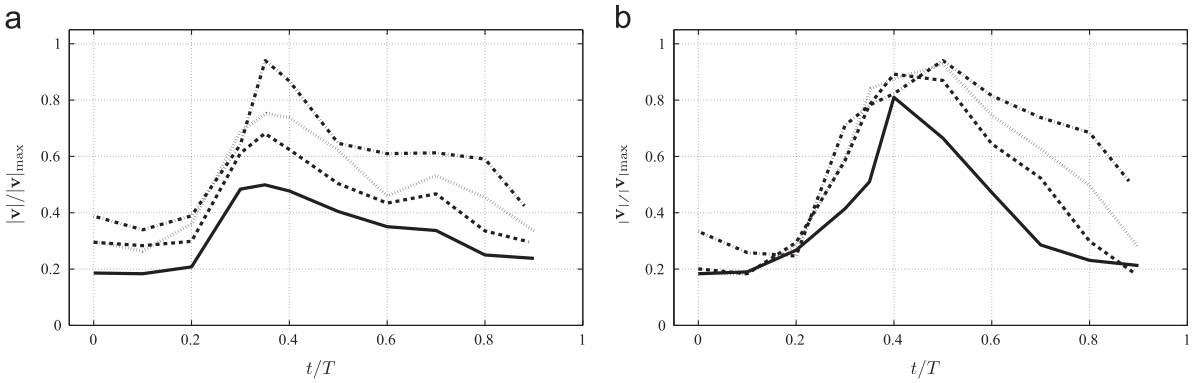

Fig. 7. Evolution of the maximum velocities caused by plates with curvatures $\kappa = 0.0$ (a), and 2.0 m^{-1} (b). Individual curves correspond to pulsatile outputs for which V_s=45 cm^3 and $f =$ 40 ppm (—), 60 ppm (- - -), 70 ppm (.....), 90 ppm (· — · —·).

substantially weaker in the case of the curved plate. Also the plots show an evident time shift: with the flat plate the peaks take place at $t/T \approx 0.35$, while with the curved plate the peaks occur with a $\Delta t/T = 1.5$ delay. More importantly, the maximum velocities remain high much longer in the case of the curved plate, as can be seen in Fig. 7(b). Finally, a comparative view of all curvatures is presented in Fig. 8 for a flow rate corresponding to 45 cm^3 and f=70 ppm. The previously mentioned effects (i.e. velocity increase and time delay) caused by the curvature are evident in this plot. It should be noted that a somewhat higher peak value occurs for the curved plate S4 (with $\kappa = 4.0$ m^{-1}).

Based on this evidence, we may conjecture that the shapes of the curves are determined by the bending characteristics of the (stiffer) curved plates. As the fluid is set into motion, the plate is deflected from its rest configuration at a rate dictated by its bending properties. Initially the flow velocity and the deflection rate have roughly the same order of magnitude $U|_{t/T<0.2} \sim \delta/t_p$. However, the bulk of the fluid continues to accelerate, while the plate's motion remains somewhat limited. Beyond a certain point only the outer corners of the curved plate continue to bend, and the fluid is forced to flow through a narrower cross section. At this point the plate's material is incapable of sustaining the increasing internal stresses (i.e. a critical loading condition is attained) and it buckles. As a result the cross section suddenly expands, leading to a decrease of the velocity. Past the mid-cycle the swirls contribute to progressively restore the plate to its original, undeformed state.

Similarly, Fig. 9(a) and (b) illustrates the effects of the curvature and the flow rate on the absolute values of the stress. A more dramatic evolution is observed in both cases as $f \to 90$ ppm. For instance, no asymptotic value is clearly discernible in either case (i.e. with or without curvature), and the peak values occur within the smaller time interval $0.3 \le t/T \le 0.4$. Furthermore, contrary to the characteristic evolution of the velocity, the peak stresses occur slightly sooner (at around $t/T = 0.35$) when curved plates are used. It is interesting to note that plates with $\kappa = 2.0$ m^{-1} have a different behavior when subjected to flows with f=70 ppm. Their induced maximum stress occur at $t/T = 0.4$, and their values decay at a slower rate throughout the remaining part of the cycle. It is evident, nonetheless, that stress values have an increasing trend that is strongly dependent on the plate's curvature.

Plots for different curvatures are shown in Fig. 10 for V=45 cm^3 and f=40 ppm. Here we also observe how plate S4 ($\kappa = 4.0$ m^{-1}) shows a different behavior. Its corresponding peak value is significantly lower when compared with those cases where a sudden collapse of the plate is observed (the plot drops past $t/T = 0.4$).

These results indicate that fluid particles would suffer the highest stresses just before the mid-cycle is reached. Furthermore, fluid particles would be exposed to such stress levels for approximately $0.2T$. Thus, lowering the curvature to prevent the formation of high velocity jets is crucial to avoiding unnecessary shearing in the fluid and surrounding structures. Milder stresses are also favored by the faster decaying rates associated with intermediate curvatures. Such considerations should be taken into account, together with the fact that the curvature is also necessary for proper valve performance in certain applications, such as valve prostheses.

5. Conclusions

Experiments were conducted to determine the particular features of the flow around flexible plates (or leaflets) with different curvatures. Due to the transient nature of the flows, the velocities were measured with a time resolved PIV system, and a phase-locking technique which allowed for a synchronized sampling of consecutive cycles. The rate-of-strain, vorticity, and the stress fields, were subsequently obtained from the velocity measurements.

The main finding of the study is that low-to-moderate curvatures induce higher stresses in the flowfield than flat plates do. Furthermore, the duration of high velocity and stress levels is also observed to increase with the curvature (unless a premature collapse occurs). With curved plates, however, the peak values do not occur synchronously. This means that peak stresses have a tendency to occur earlier during the cycle than peak velocities. In spite of these differences, all maxima occur within the interval $0.3 \le t/T \le 0.5$. Also, it must be emphasized that large curvatures do not necessarily lead to higher induced stress levels, since a sudden collapse may take place before the conditions are met to produce them.

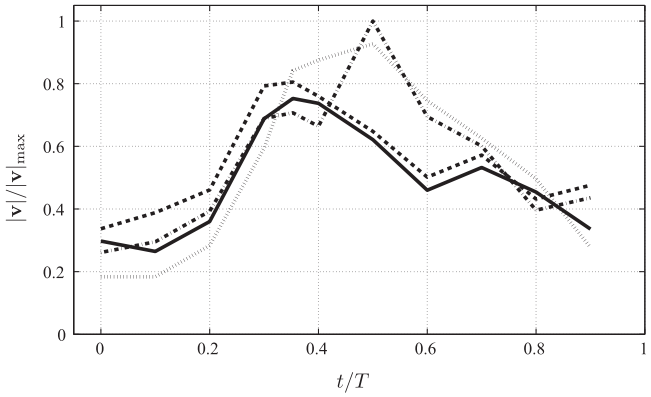

Fig. 8. Comparison of the maximum velocities caused by plates with curvatures $\kappa =$ 0.0 m^{-1} (—), 1.0 m^{-1} (- - -), 2.0 m^{-1} (.....), 4.0 m^{-1} ($\cdot - \cdot - \cdot$). The flow rate corresponds to V_s=45 cm^3 and f=70 ppm.

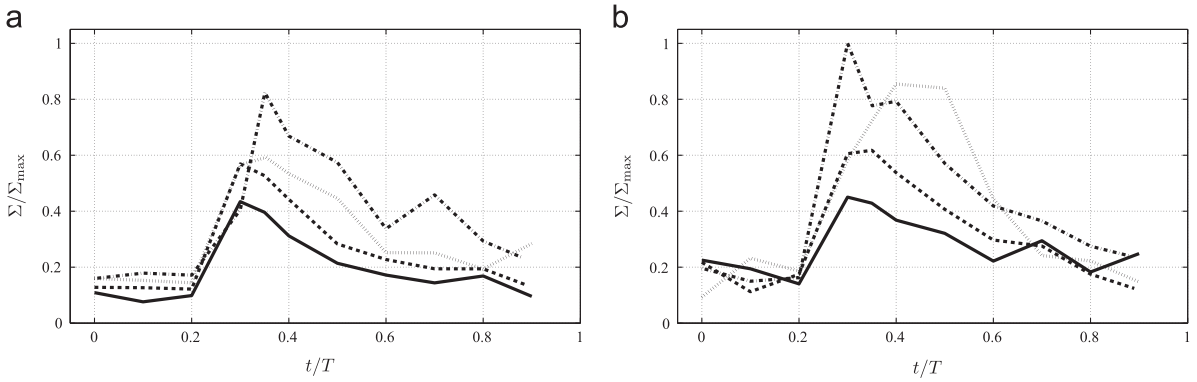

Fig. 9. Evolution of the stresses for plates with curvatures $\kappa = 0.0$ and 2.0 m^{-1}. Individual curves correspond to a flow rate with V_s=45 cm^3 and f= 40 ppm (—), 60 ppm (- - -), 70 ppm (.....), 90 ppm ($\cdot - \cdot - \cdot$).

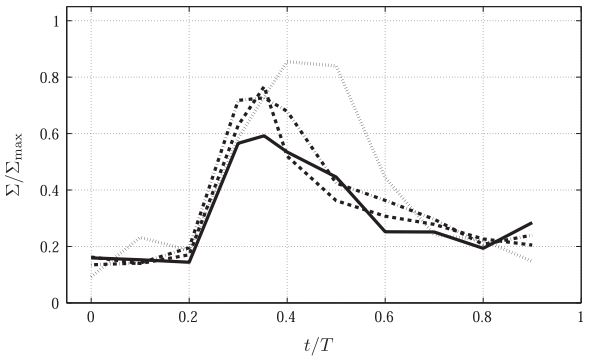

Fig. 10. Global comparison of the stresses caused by plates with curvatures $\kappa =$ 0.0 m^{-1} (—), 1.0 m^{-1} (- - -), 2.0 m^{-1} (.....), 4.0 m^{-1} ($\cdot - \cdot - \cdot$). The flow rate corresponds to V_s=45 cm^3 and f=70 ppm.

The following points should be remarked when considering the general characteristics of the flowfield: (a) The flow around curved plates shows a much wider distribution of secondary eddies. Less compact swirls are also evident in the case of curved plates, in particular the (large) vortex-like circulations being shed to the wake just downstream from the valve; (b) Those regions with highest stressing potential are located at the upper and lower wall of the channel. The upper wall is specially prone to severe shearing due to the presence of the jet impinging on it during the initial stages of the cycle, and develops much further downstream than any other layer; (c) It is observed that the boundary layers generated on the upstream surface of the plates evolve into vortex-like structures that eventually detach and are advected downstream by the main flow; (d) The effects associated with the secondary flows generated around the plates' edges, and the boundary layers developed at the walls, may become relevant depending on the size of the plates.

This study is a continuation of previous investigations aimed at understanding the influence that diverse parameters have on the flow properties of prosthetic valves (Ledesma-Alonso et al., 2014; López-Zazueta et al., 2011). It is remarked that, despite the crucial role played by the curvature on the evolution of the flow (Butcher et al., 2011), additional experiments are still required to fully reveal the extent of its influence. In addition, modeling the three dimensional behavior of such systems is a task far from trivial due to the fact that the flow is unsteady, and because there is a strong two-way coupling between the flow and the structure. In spite of this, an experimental description of the flow features may still be helpful during the design stage of prosthetic heart valves.

Acknowledgments

This study was financially supported by CONACyT through Project No. 102507.

References

Arellano Castro, R.F., Guillamont, L., Cros, A., Eloy, C., 2014. Non-linear effects on the resonant frequencies of a cantilevered plate. Journal of Fluids and Structures 46, 165–173.
Bidkar, R.A., Kimber, M., Raman, A., Bajaj, A.K., Garimella, S.V., 2009. Nonlinear aerodynamic damping of sharp-edged flexible beams oscillating at low Keulegan–Carpenter numbers. Journal of Fluid Mechanics 634, 269–289.
Bluestein, D., Rambod, E., Gharib, M., 2000. Vortex shedding as a mechanism for free emboli formation in mechanical heart valves. Journal of Biomechanical Engineering 122, 125–134.
Butcher, J.T., Mahler, G.J., Hockaday, L.A., 2011. Aortic valve disease and treatment: the need for naturally engineered solutions. Advanced Drug Delivery Review 1, 1–27.
Carra, S., Amabili, M., Garziera, R., 2013. Experimental study of large amplitude vibrations of a thin plate in contact with sloshing liquids. Journal of Fluids and Structures 42, 88–111.
Diourté, B., Siché, J.P., Comparat, V., Baguet, J.P., Mallion, J.M., 1999. Study of arterial blood pressure by a Windkessel-type model: influence of arterial functional properties. Computer Methods and Programs in Biomedicine 60, 11–12.
Eloy, C., Lagrange, R., Souilliez, C., Schouveiler, L., 2008. Aeroelastic instability of cantilevered flexible plates in uniform flow. Journal of Fluid Mechanics 611, 97–106.
Facci, A.L., Porfiri, M., 2013. Analysis of three-dimensional effects in oscillating cantilevers immersed in viscous fluids. Journal of Fluids and Structures 38, 205–222.
Faltinsen, O.M., 2000. Hydroelastic slamming. Journal of Marine Science and Technology 5, 49–65.
Garitey, V., Gandelheid, T., Fusezi, J., Pelissier, R., 1995. Ventricular flow dynamic past bileaflet prosthetic heart valves. International Journal of Artificial Organs 18, 380–391.
Giersiepen, M., Wurzinger, L.J., Opitz, R., Reul, H., 1990. Estimation of shear stress-related blood damage in heart valve protheses—in vitro comparison of 25 aortic valves. International Journal of Artificial Organs 13 (5), 300–306.
Gluck, M., Breuer, M., Durst, F., Halfmann, A., Rank, E., 2001. Computation of fluid structure interaction on lightweight structures. Journal of Wind Engineering 89, 1351–1368.
Gosselin, F., Langre, E., Machado-Almeida, B., 2010. Drag reduction of flexible plates by reconfiguration. Journal of Fluid Mechanics 650, 319–341.
Grigioni, M., Daniele, C., D'Avenio, G., Barbaro, V., 2001. The influence of the leaflets' curvature on the flow field in two bileaflet prosthetic heart valves. Journal of Biomechanics 34, 613–621.
He, G., Kashiwagi, M., 2010. Nonlinear analysis on wave-plate interaction due to disturbed vertical elastic plate. Journal of Hydrodynamics 22 (5), 507–512.
Hellums, D., 1994. 1993 Whitaker lecture: biorheology in thrombosis research. Annals of Biomedical Engineering 22, 445–455.
Howell, R.M., Lucey, A.D., Pitman, M.W., 2011. The effect of inertial inhomogeneity on the flutter of a cantilevered flexible plate. Journal of Fluids and Structures 27, 383–393.
Ihara, A., Watanabe, H., 1994. On the flow around flexible plates oscillating with large amplitude. Journal of Fluids and Structures 8, 601–619.
Jang, G.W., Chang, S.M., Gim, G.H., 2013. Fluid–structure interaction of quasi-one-dimensional potential flow along channel bounded by symmetric cantilever beams. Journal of Fluids and Structures 40, 127–147.
Kim, Y., Wereley, S.T., Chun, C., 2004. Phase-resolved flow field produced by a vibrating cantilever plate between two endplates. Physics of Fluids 16, 145–162.
Ledesma-Alonso, R., Guzmán, J.E.V., Zenit, R., 2014. Experimental study of a model valve with flexible leaflets in a pulsatile flow. Journal of Fluid Mechanics 739, 338–362.
Lee, J., Lee, S., 2012. Fluid–structure interaction analysis on a flexible plate normal to a free stream at low Reynolds numbers. Journal of Fluids and Structures 29, 18–34.
López-Zazueta, A., Ledesma-Alonso, R., Guzmán, J.E.V., Zenit, R., 2011. Study of the velocity and strain fields in the flow through prosthetic heart valves. Journal of Biomechanical Engineering 133, 121003–121010.
Lucey, A.D., Cafolla, G.J., Carpenter, P.W., Yang, M., 1997. The nonlinear hydroelastic behavior of flexible walls. Journal of Fluids and Structures 11, 717–744.
Pedrizzetti, G., Domenichini, F., 2006. Flow-driven opening of a valvular leaflet. Journal of Fluid Mechanics 569, 321–330.
Peterson, S.D., Porfiri, M., Rovardi, A., 2009. A particle image velocimetry study of vibrating ionic polymer metal composites in aqueous environments. IEEE/ASME Transactions on Mechatronics 14, 474–483.
Phan, N.C., Aureli, M., Porfiri, M., 2011. Finite amplitude vibrations of cantilevers of rectangular cross section in viscous fluids. Journal of Biomechanical Engineering 133, 121003–121010.
Porfiri, M., Peterson, S., 2013. In: Advances in Energy Harvesting Methods1st edition Springer, New York.
Prince, C., Lin, W., Lin, J., Peterson, S.D., Porfiri, M., 2010. Temporally-resolved hydrodynamics in the vicinity of a vibrating ionic polymer metal. Journal of Applied Physics 107, 1–12.
Sallam, A.M., Hwang, N.H.C., 1984. Human red blood hemolysis in a turbulent shear flow: contribution of Reynolds shear stresses. Biorheology 21, 783–797.
Taylor, R.E., Ohkusu, M., 2000. Green functions for hydroelastic analysis of vibrating free-free beams and plates. Applied Ocean Research 22, 295–314.
Thiriet, M., 2008. Biology and Mechanics of Blood Flows, Part II: Mechanics and Medical Aspects1st edition Springer, New York.
Tubaldi, E., Amabili, M., 2013. Vibrations and stability of a periodically supported rectangular plate immersed in axial flow. Journal of Fluids and Structures 39, 391–407.
Yamaguchi, N., Yokota, K., Yoshinobu, T., 2000. Flutter limits and behaviors of a flexible thin sheet in high-speed flow-I: analytical method for prediction of the sheet behavior. Journal of Fuids Engineering 122, 65–73.
Yoganathan, A.P., He, Z., Casey-Jones, S., 2004. Fluid mechanics of heart valves. Annual Review of Biomedical Engineering 6, 331–362.